An Ultra-Fast Intrinsic Contact Sensing Method for Medical Instruments With Arbitrary Shape

Guanglin Cao, Mingcong Chen, Jian Hu, and Hongbin Liu, *Member, IEEE*

***Abstract*—Intraoperative contact sensing has the potential to reduce the risk of surgical errors and enhance manipulation capabilities for medical robots, particularly in contact force control. Current intrinsic force sensing (IFS) methods are limited in application to medical instruments with arbitrary shape, due to high computational time and reliance on surface equations. This study presents an ultra-fast IFS method that uses multiple planes to establish surface geometry descriptions. The method can reduce high-order contact mechanical models that need to be solved iteratively to a set of linear equations, and calculate contact location analytically. In addition, a robot motion control approach based on the contact sensing method is proposed to maintain stable contact force and regulate the probe's orientation for robotic ultrasound systems (RUSS). Experimental results show that the contact sensing method is robust to friction and can achieve a mean (±SD) displacement error of 1.04 ± 0.43 mm in contact location with computational time less than 1 ms. The system has been evaluated on a phantom with sinusoidal motion. To the best of our knowledge, this is the first study to validate adaptiveness of RUSS under dynamic conditions. The results demonstrated that the system exhibits comparable manipulation capabilities to human operators with only force sensing, indicating a high level of adaptiveness.**

***Index Terms*—Force control, force and tactile sensing, medical robots and systems.**

Manuscript received 14 April 2023; accepted 15 August 2023. Date of publication; date of current version. This letter was recommended for publication by Associate Editor M. Tavakoli and Editor J. Burgner-Kahrs upon evaluation of the reviewers' comments. This work was supported by InnoHK Program. *(Corresponding author: Hongbin Liu.)*

Guanglin Cao is with the State Key Laboratory of Multimodal Artificial Intelligence Systems, Institute of Automation, Chinese Academy of Sciences, Beijing 100190, China, also with the Centre for Artificial Intelligence and Robotics, Hong Kong Institute of Science and Innovation, Chinese Academy of Sciences, Hong Kong, and also with the School of Artificial Intelligence, University of Chinese Academy of Sciences, Beijing 100049, China (e-mail: caoguanglin2021@ia.ac.cn).

Mingcong Chen and Jian Hu are with the State Key Laboratory of Multimodal Artificial Intelligence Systems, Institute of Automation, Chinese Academy of Sciences, Beijing 100190, China, and also with the Centre for Artificial Intelligence and Robotics, Hong Kong Institute of Science and Innovation, Chinese Academy of Sciences, Hong Kong (e-mail: mingcong.chen@cair-cas.org.hk; hujian@ia.ac.cn).

Hongbin Liu is with the State Key Laboratory of Multimodal Artificial Intelligence Systems, Institute of Automation, Chinese Academy of Sciences, Beijing 100190, China, also with the Centre for Artificial Intelligence and Robotics, Hong Kong Institute of Science and Innovation, Chinese Academy of Sciences, Hong Kong, and also with the School of Biomedical Engineering and Imaging Sciences, King's College London, SE1 7EU London, U.K. (e-mail: liuhongbin@ia.ac.cn).

This letter has supplementary downloadable material available at https://doi.org/10.1109/LRA.2023.3313067, provided by the authors.

Digital Object Identifier 10.1109/LRA.2023.3313067

I. Introduction

ROBOT-ASSISTED surgery has revolutionized medical fields by enabling minimally invasive procedures, highly precise operations, faster recovery times, and fewer complications [1]. The utilization of robotic arms to hold medical instruments can free clinicians from labor-intensive tasks and significantly enhance surgical skills. During interaction between medical instruments and patients, precise sensing of contact information (usually the magnitude and location of force) facilitates better manipulation, as illustrated in Fig. 1. The contact force and angle between ultrasound (US) probes and the target skin are crucial factors for robotic ultrasound systems (RUSS) to obtain reliable US image. Ensuring the proper angle and intensity of bone grinding during robotic knee replacement surgery is essential to avoid implant malalignment and improve patient outcomes [2]. Real-time sensing of endoscope blind spots and tissue contact during transnasal endoscopic surgery can provide more precise manipulation to mitigate risks and promote patient safety. While humans can readily perceive contact information with their hands, possessing such an ability is a constant challenge for medical robots.

The achievement of contact sensing in medical instruments typically involves extrinsic and intrinsic sensing methods [3]. Extrinsic sensors located in or near the contact area can avoid the attenuation of force along the way, including micro pressure sensors [4] as well as flexible tactile skin [5]. While sensor-based methods are intuitive and precise, they have limitations in terms of size, reliability, and versatility. Most sensors are only suitable for regular surfaces, requiring redesigns for each medical instrument [6].

Intrinsic force sensing (IFS) methods can indirectly obtain contact information through force and torque (F/T) measurement and geometric surface descriptions of instruments [7]. It is well-established and has been widely verified in practical robotic applications, such as dexterous hand manipulation [8], [9], [10], surface haptic exploration [11], [12] and collision avoidance during human-robot interaction [13], [14]. Bicchi et al. conducted a survey of various contact models and presented theoretical analyzes along with solutions for intrinsic contact sensing [15]. The contact point is located where the wrench-axis intersects the object surface, in which the wrench-axis is a unique line along with force and parallel to moment [16]. However, this method can only cope with point contact on rigid surfaces. Liu et al. considered deformation and achieved good accuracy even at high friction by implementing an iterative algorithm [8]. Back et al. proposed a surface following control algorithm for the contact sensing finger [11]. To further expand the application

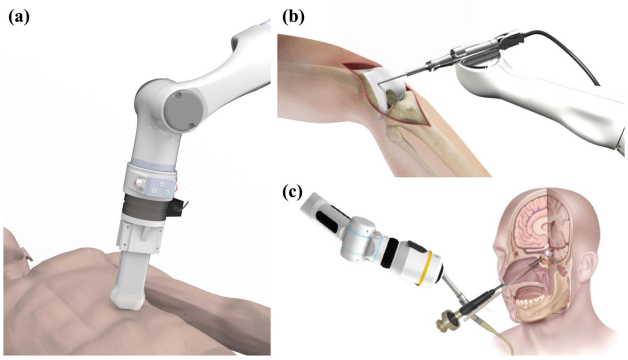

Fig. 1. Examples of interaction between medical instruments and tissues. (a) Robotic ultrasound systems. (b) Robotic system for knee replacement surgery. (c) Robotic system for transnasal endoscopic surgery.

of explore objects with dynamic movements, Sun et al. proposed an adaptive force and velocity control algorithm [12]. Ciotti et al. presented an iterative procedure that relies on force-deformation characteristics of the contact to achieve a better exploration of unknown environments [7].

Nevertheless, the iterative solution for high-order contact mechanical models is time-consuming, making it unsuitable for real-time applications. Kim et al. placed six-axis F/T sensors between the cover and the link of the robot manipulator, utilizing the IFS algorithm to acquire abundant contact information. An analytical solution for the contact location was obtained by assuming the robot link as a cylindrical surface [14]. Based on contact sensing methods, robot manipulators can effectively control the motion of robot end-effector to prevent human injury due to physical contacts [17]. However, these methods require precise descriptions (usually three-dimensional nonlinear equations) of object surfaces. For medical instruments with complex surfaces such as US probes, constructing accurate descriptions is a challenging task. Additionally, utilizing contact sensing feedback to enhance the control of medical instrument motion also presents a challenge.

This study presents an ultra-fast contact sensing method for medical instruments with arbitrary shape. The contact location is calculated using an intrinsic force sensing algorithm relies entirely on F/T measurement and geometric surface descriptions of medical instruments. Compared to the previous studies, the novelty of the contact sensing method proposed in this letter is twofold: (1) establishing the geometric description by a multi-plane fitting approach, thus the algorithm can be applied to medical instruments with arbitrary shape, (2) reducing high-order contact mechanical models to a set of linear equations and calculating contact location analytically. Additionally, the multi-plane fitting approach can be easily implemented using mesh models. The novel IFS algorithm reduces computational time and enables quick calculations (within 1 ms), demonstrating its potential application in real-time contact sensing and robot motion control for medical robots. To verify the feasibility of the proposed method, we developed a robotic ultrasound system (RUSS) and evaluated the accuracy of contact location detection and computational time across three commonly-used ultrasound (US) probes (linear probe, convex probe and T-shaped probe). Further validation of the robustness was conducted by assessing the impact of different contact angles (simulated friction) and forces on the accuracy of detection. In addition, to fully demonstrate the enhanced capability of real-time contact sensing in robotic manipulation, we proposed a motion control framework that enables RUSS to maintain constant contact forces and angles between the US probe and target skin in challenging out-of-hospital settings, such as ambulances. The performance of the system is evaluated by conducting experiments on a soft phantom under dynamic conditions.

II. Methodology

In this work, the robot end-effector is connected to a six-axis F/T sensor, which is mounted with US probes. The contact force applied to the probe was detected with the force sensor, and the motion of the probe was controlled with the robot manipulator.

A. System Calibration and Force Compensation

To ensure accurate contact sensing and contact force and angle control, a system coordinates calibration must be conducted based on the mechanical configuration. The transformation from the world coordinate to the F/T sensor coordinate is determined by the mechanical design and can be expressed as ${}^S_W R = {}^B_W R \cdot {}^E_B R \cdot {}^S_E R$, where W denotes the world frame, B denotes the robot base frame, E denotes the robot end-effector frame, and S denotes the F/T sensor frame, as shown in Fig. 5(a). In this configuration, B has the same orientation as W, while S has the same orientation as E and ${}^E_B R$ can be calculated from robot forward kinematics. The gravity of the US probe needs to be compensated to obtain the accurate contact force between the probe and human skin. Therefore, the prestress of the F/T sensor and the weight center of the probe should be estimated in advance. The F/T sensor utilized in this work is a commercially accessible sensor known for its precision measurements. Based on the F/T measurements, the contact force and torque are satisfied with the following equations,

$$\begin{aligned} F_e &= F_s - {}^S_W R \cdot {}^W G - F_0 \\ M_e &= M_s - {}^S Lg \times {}^S G - M_0 \end{aligned} \tag{1}$$

where F_e, M_e are the contact force and torque between the probe and human skin, respectively; F_0, M_0 are initial readings of the F/T sensor; F_s, M_s are current outputs from the F/T sensor; G is the load weight and Lg is the load weight centre. With the data of F_s, M_s and ${}^S_W R$ in more than three different non-contact poses, the unknown parameters F_0, M_0, G, Lg are satisfied with the following equations,

$$\begin{cases} F_{s1} = {}^S_W R_1 \cdot {}^W G + F_0 \\ M_{s1} = {}^S Lg \times (F_{s1} - F_0) + M_0 \\ F_{s2} = {}^S_W R_2 \cdot {}^W G + F_0 \\ M_{s2} = {}^S Lg \times (F_{s2} - F_0) + M_0 \\ \cdots \\ F_{sn} = {}^S_W R_n \cdot {}^W G + F_0 \\ M_{sn} = {}^S Lg \times (F_{sn} - F_0) + M_0 \end{cases} \tag{2}$$

where n is the number of non-contact poses. These parameters can be calculated by the Least-squares method from [18]. Based on it, F_e and M_e can be calculated in real time during the robot

IEEE Robotics and Automation Letters (RA-L) paper, presented at ICRA 2024, Yokohama, Japan. Cite as RA-L paper.

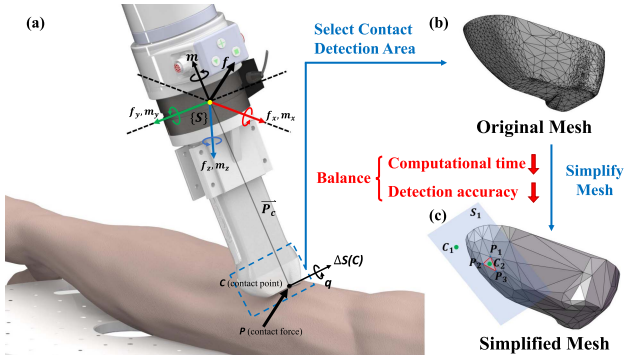

Fig. 2. (a) The F/T measurement of the applied force at a contact point and methods for computational time reduction. (b) Original Mesh. (c) Simplified Mesh and location constraint.

Algorithm 1: Intrinsic Force Sensing.

Input: F/T Measurement; Medical Instruments mesh model
Calculate surface equations $S_1, S_2, \ldots, S_n$ and normal vectors $N(S_1), N(S_2), \ldots, N(S_n)$ ▷ Initialization
$F_e = [f_x, f_y, f_z]^T$ $M_e = [m_x, m_y, m_z]^T$ ▷ Read sensor
repeat
  $g(F_e, M_e, S_i, p_c) = 0 \Rightarrow AX = B$
  solve $X = A^{-1}B$, where $X = [x, y, z, k]^T$
  $p_c = [x, y, z]^T$
until $(F_e \cdot N(S_i) \leq 0) \wedge (p_c \in S_i)$ ▷ Plane constraint
Output: p_c ▷ Coordinates of contact location in sensor frame

motion from (1). Additionally, a Kalman filter is integrated into the contact force calculation to eliminate the noise due to the robot motor vibrations and sensor drift [19]. Gravity compensation is a linear model that relies solely on the current robot pose and sensor readings. Therefore, we incorporate a Kalman filter to smooth the real contact force after gravity compensation, thereby enhancing the smoothness of robot motion control. An identity matrix is used as the transition matrix for the measured and estimated F/T value. The state error and measurement error involved in the model is empirically chosen to be $\mathcal{N}(0, 10^{-6})$ and $\mathcal{N}(0, 2 \times 10^{-4})$, respectively.

B. Contact Sensing Algorithm

Due to the soft contact between the medical instruments and tissues, the contact force distribution on the limited contact area is subject to complex continuum mechanics, rendering its calculation beyond the real-time sensing requirements. Bicchi proved that if two applied forces yield the same large-scale effect, they can be regarded as equivalent [15]. Consequently, the contact model can be approximated as a resultant force/torque acting on a single point, namely the contact centroid. This point has a unique solution for a specific type of contact. As shown in Fig. 2(a), applying a force p at a point $p_c = [x, y, z]^T$ can get F_s and M_s from F/T sensor and F_e, M_e from (1). The US probe will generate an acceleration $\ddot{x}$ and an angular acceleration $\ddot{\omega}$, which satisfies the force and moment equilibrium equations,

$$\begin{cases} F_e - p = m\ddot{x} \\ M_e - p_c \times p + q = I\ddot{\omega} \end{cases} \tag{3}$$

where m is the mass, I is the moment of inertia, q is the local torque due to deformation. q is always parallel to the normal vector of the contact surface. Thus, the local torque at contact point p_c can be expressed as $q = k\nabla S(p_c)$, where ∇ represents the gradient operator, $\nabla S(p_c)$ is the normal vector of the contact location and k is an unknown constant. The multi-plane fitting approach is utilized to establish the surface equation of medical instruments with arbitrary shape, resulting in geometric descriptions of the surface composed of a set of plane equations $S_1, S_2, \ldots, S_n$. When the US image is acquired, the probe can be seen as static so that $\ddot{x}$ and $\ddot{\omega}$ is approximate to 0. The contact point p_c needs to satisfy the following equations,

$$\begin{cases} M_e - p_c \times F_e + kN(S_i) = 0 \\ S_i(p_c) = 0 \end{cases} \tag{4}$$

where $S_i(p_c) = a_i x + b_i y + c_i z + d_i$ is the surface equation, $N(S_i) = [a_i, b_i, c_i]^T$ is the normal vector of the surface. The expansion of the above equations can be written as a set of linear equations,

$$\boldsymbol{g}(F_e, M_e, S_i, p_c) = \begin{bmatrix} a_i k - f_y z + f_z y - m_x \\ b_i k - f_z x + f_x z - m_y \\ c_i k - f_x y + f_y x - m_z \\ a_i x + b_i y + c_i z + d_i \end{bmatrix} = 0 \tag{5}$$

Let $X = \begin{bmatrix} x, y, z, k \end{bmatrix}^T$, the linear equations can be explained as a matrix equation $AX = B$.

$$A = \begin{bmatrix} 0 & f_z & -f_y & a_i \\ -f_z & 0 & f_x & b_i \\ f_y & -f_x & 0 & c_i \\ a_i & b_i & c_i & 0 \end{bmatrix} X = \begin{bmatrix} x \\ y \\ z \\ k \end{bmatrix} B = \begin{bmatrix} m_x \\ m_y \\ m_z \\ -d_i \end{bmatrix} \tag{6}$$

For each mesh plane, the above equation has a unique solution unless the plane passes through the F/T sensor origin. However, the validity of this solution needs to be determined based on the two constraints. Firstly, it is necessary to constrain the solution to lie on the actual surface of the medical instrument. As shown in Fig. 2(c), since no positional constraints are imposed while solving (5), for the mesh plane S_1, the solution could be either C_1 or C_2. However, C_1 does not lie within the interior of triangle $P_1P_2P_3$, rendering it an invalid solution. This constraint is satisfied when the contact point and every vertex of the mesh plane are on the same side of the line formed by the remaining two vertices. Additionally, the normal vector direction of the mesh plane must be opposite to the force direction because medical instruments are under pressure from tissues. The developed algorithm is illustrated in pseudo code as shown in Algorithm 1.

To simplify the implementation of the contact sensing algorithm, it is recommended to align the coordinate origin of the mesh model of the medical instruments with the F/T sensor origin, so that no coordinate transformation is required. To further minimize the computational time, we propose the following

IEEE Robotics and Automation Letters (RA-L) paper, presented at ICRA 2024, Yokohama, Japan. Cite as RA-L paper.

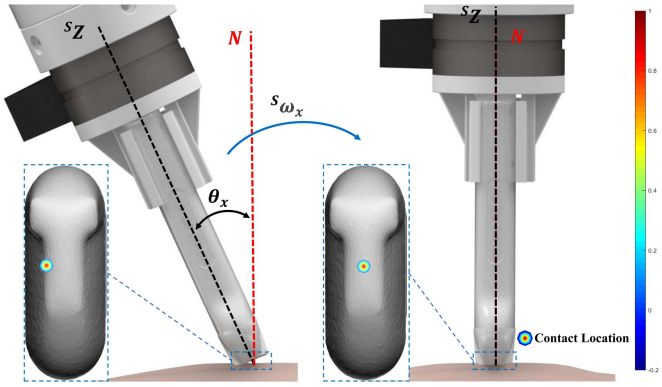

Fig. 3. Example of out-of-plane scan angle adjustment based on contact location. The symbols N and ${}^{S}Z$ represent normal vector of target skin and the centre line of US probe, respectively. ${}^{S}\omega_x$ is the angular velocity of rotation in ${}^{S}X$ (out-of-plane) to compensate the angle θ_x between N and ${}^{S}Z$.

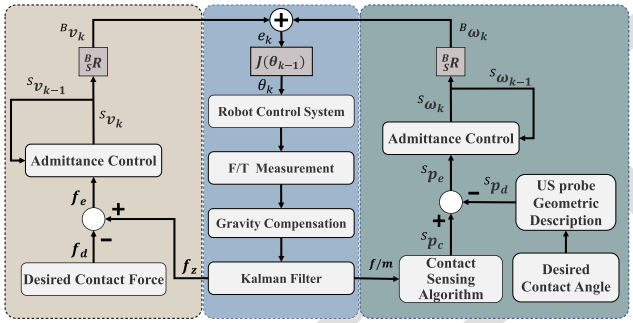

Fig. 4. Motion control framework, including contact force control and probe orientation adjustment with admittance controller based on the contact sensing algorithm.

methods as illustrated in Fig. 2. Firstly, simplify the mesh model but this may result in a loss of accuracy. Therefore, it is crucial to balance between detection accuracy and computational time. In addition, it is advisable to detect only those regions where contact is likely to occur, thereby reducing the number of mesh planes.

C. Robot Motion Control

The proposed real-time contact sensing algorithm has potential applications in contact information feedback to clinicians as well as in the motion control for medical robots. In this work, we proposed a novel approach for adjusting the orientation of US probes based on the contact location error. Fig. 3 illustrates an orientation adjustment example, in which center scan line of the US probe is aligned perpendicularly with the target surface. This alignment is achieved by controlling the contact location so that it remains at the geometric center of the probe. Furthermore, to achieve constant contact force and angle control in challenging out-of-hospital settings, a motion control approach based on admittance controller is presented in Fig. 4. Admittance controller has been widely employed for interaction control, which can enhance the smoothness of robot motion. The contact force error is used to maintain the desired contact force, while the contact location error is employed to control the orientation of the probe.

To maintain the desired force f_d, the current contact force f_z is used as feedback of the admittance controller to adjust the position of the probe along the Z axis. The force error $f_e = f_z - f_d$ and the probe velocity of the last control cycle are the inputs,

$$M_f \frac{\left({}^{S}v_k - {}^{S}v_{k-1}\right)}{\Delta t} + D_f \left({}^{S}v_{k-1} - 0\right) = f_z - f_d \quad (7)$$

where $M_f, D_f \in \mathbb{R}^3$ represent mass and damping parameters in force control, and Δt is the control interval. The velocity ${}^{S}v_k \in \mathbb{R}^3$ can be obtained from (7).

The desired contact angle between the probe and target skin is used to determine the desired contact location ${}^{S}p_d$. The current contact location ${}^{S}p_c$ from contact sensing method is used as feedback of the admittance controller to adjust the orientation of the probe. The contact location error ${}^{S}p_e = {}^{S}p_c - {}^{S}p_d$ and the probe angular velocity of the last control cycle are the inputs to the admittance controller,

$$M_p \frac{\left({}^{S}\omega_k - {}^{S}\omega_{k-1}\right)}{\Delta t} + D_p \left({}^{S}\omega_{k-1} - 0\right) = {}^{S}p_c - {}^{S}p_d \quad (8)$$

where $M_p, D_p \in \mathbb{R}^3$ represent mass and damping parameters in orientation control. The angular velocity ${}^{S}\omega_k \in \mathbb{R}^3$ can be obtained from (8). Thus, the difference between the probe current pose and target pose in robot base frame $e_k \in \mathbb{R}^6$ can be obtained,

$$e_k = \left[{}^{B}_{S}R \cdot (S_z \odot {}^{S}v_k), \quad {}^{B}_{S}R \cdot (S_{xy} \odot {}^{S}\omega_k)\right]^T \quad (9)$$

where S_z and S_{xy} are two selection matrixes and $\odot$ represents element-wise multiplication (Hadamard product). The contact force was controlled through the contact depth adjustment, and the out-of-plane and in-plane contact angles could be controlled by the x-axis and y-axis contact location error. Therefore, $S_z = [0, 0, 1]^T$ and $S_{xy} = [1, 1, 0]^T$. The robot arm joints $\theta_k \in \mathbb{R}^6$ in control cycle k is the control signal for the robot servo system, which is expressed as

$$\theta_k = \theta_{k-1} + (J^T(\theta_{k-1})J(\theta_{k-1}) + \lambda^2 I)^{-1} J^T(\theta_{k-1}) e_k \quad (10)$$

where $J(\theta_k) \in \mathbb{R}^{6\times6}$ represents robot Jacobian matrix and λ is a non-zero damping constant [20]. Therefore, at each control cycle, the current contact force and joints are the inputs of the motion control framework and joints of the next motion is the output. The robot automatically adjusts the contact force and angle in response to environmental changes to optimize the quality of US images.

III. Experiments

A. Experimental Setup

The robotic ultrasound system contains three main components: a six-axis robot arm (Elfin3, Hans Robot, China), a six-axis force/torque sensor (M3815B, SRI Sensor, China) and a T-shaped wireless US probe (Cprobe, Sonostar, China), as shown in Fig. 5(a). The US probe, the F/T sensor and the end-effector of the robot are connected together via custom 3-D printed connectors (Material ABS, Stratasys F170, USA). Algorithms for contact sensing and robot motion control are implemented by C++ on an Intel Core i7-11700H 2.50 GHz PC with 16 GB RAM.

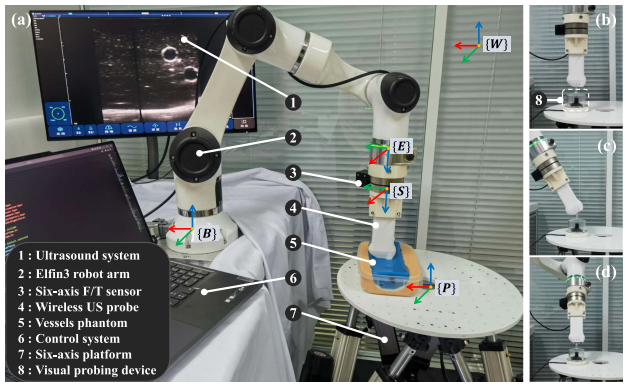

Fig. 5. System setup of a dynamic experiment and coordinate define.

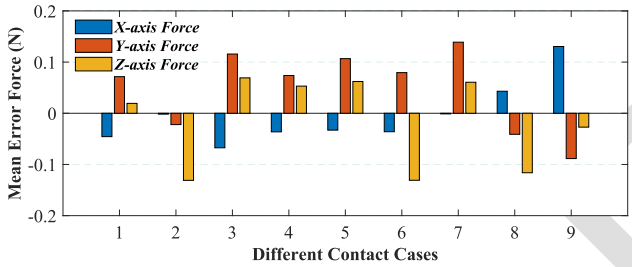

Fig. 6. Mean force error between the force reference and the contact force in different contact cases.

The robot controller and the F/T sensor are working at 50 Hz and 200 Hz, respectively. Scanning experiments were conducted on a soft phantom with flat surface, which is mounted on a six-axis platform (LJ-6D-06, Nanjing Lingjin Automation Equipment, China). The six-axis platform can provide 6-DOF motion which is used to simulate the dynamic environments.

B. Performance Evaluation of Contact Sensing Algorithm

A specialized experimental platform was devised, as depicted in Fig. 5(b). The 3D model of the US probe establishes the positional reference, which is subsequently transferred onto the surface by utilizing a 3D printing housing to label markers, as shown in Fig. 9(b). To facilitate detection, we developed a visual probing device featuring a mark with a cross at the center of the synapse, which is constructed transparently using 3D printing technology and integrated with a camera to enable visual determination of the contact with the markers. To evaluate the accuracy of the contact force calculation, we employed an identical force sensor positioned beneath the visual probing device to directly measure the contact force as a reference value. The contact forces gradually increased from 5 N to 20 N in different contact cases with various locations and angles, and the mean force errors between the force reference and the contact force are illustrated in Fig. 6. The results indicate that the contact forces obtained by gravity compensation and Kalman filter can be regarded as dependable reference values for the applied forces.

To simulate contact conditions with friction, the probing device was attached to the platform, and the robot drove the US probe to establish angled contact. Three different contact angles

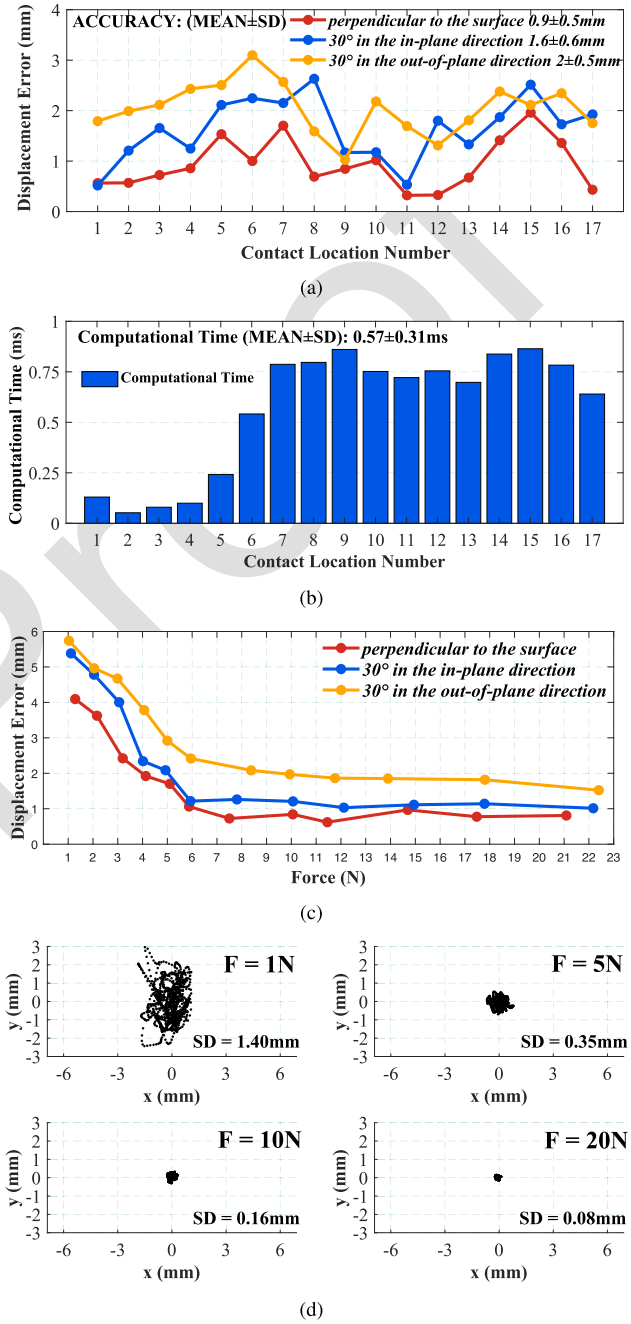

Fig. 7. (a) Displacement error in different contact angles. (b) Computational time at each marker. (c) Displacement error in different contact forces. (d) Distribution of contact location with different magnitude of contact force.

were set in the experiments, perpendicular to the surface, 30° in the in-plane direction and 30° in the out-of-plane direction as shown in Fig. 5(b), (c), and (d), respectively. The contact process was repeated three times for each marked point with each angle. The contact location and computational time were recorded when the resultant force was between 8–10 N. The displacement error and the computational time of 17 markers are shown in Fig. 7(a) and (b), respectively.

From Fig. 7(a), the contact sensing algorithm can estimate the 17 contact location accurately, with a maximum displacement error of 3.10 mm. The perpendicular contact with an accuracy

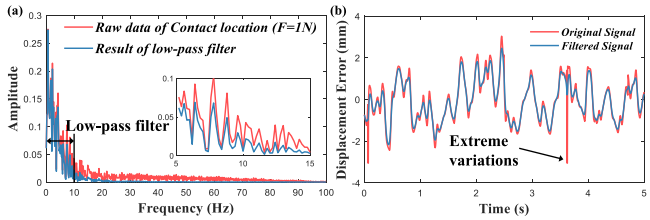

Fig. 8. (a) Fast Fourier transform analysis on contact location. (b) The original and filtered data of contact locations.

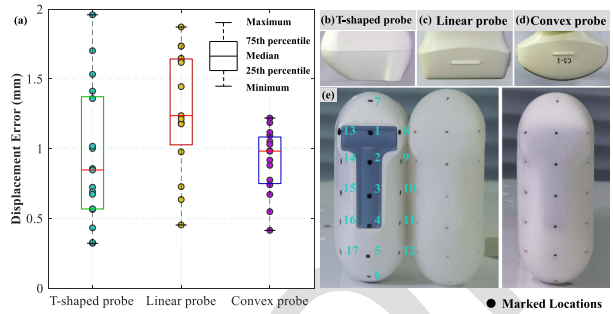

Fig. 9. (a) Displacement errors on three different probes. (b) T-shaped probe. (c) Linear probe. (d) Convex probe. (e) Marked locations on T-shaped probe.

(mean $\pm$ SD) of 0.9 $\pm$ 0.5 mm is more precise than two angled contact cases, 1.6 $\pm$ 0.6 mm (in-plane) and 2.0 $\pm$ 0.5 mm (out-of-plane). This arises due to the machining discrepancy during assembly, the establishment of the reference point, and the determination of alignment offsets based on camera images may contribute to certain inaccuracies. Additionally, since the contact location estimation method relies on the probe's 3D model, the angled contact causes friction resulting in probe position different from it in the model. In addition, the multi-plane fitting method exhibits a larger error as the probe surface becomes steeper. As a result, the accuracy of the out-of-plane angled contact case is lower than that of the in-plane case. From Fig. 7(b), the maximum computational time is 0.89 ms with a mean ($\pm$SD) of 0.57 $\pm$ 0.31 ms much less than the robot control cycle of 20 ms, which enables high-speed control. Furthermore, the computational time for markers 1–5 is significantly shorter than for other markers. Since the markers 1–5 are located in the high-frequency contact area, the mesh planes in these areas were designed to be prioritized in the algorithm for further reducing computational time.

The magnitude of the contact force applied to obtain clear US images on various tissues is different. Therefore, we evaluated the impact of different magnitude of forces on the accuracy of the contact sensing algorithm. According to the current RUSS researches, the contact force is 1 N in abdominal aorta scanning [21] and 5 N in spine and forearm blood vessels acquisition [22]. There also is an abdominal aorta scanning with 15–20 N force [23]. Therefore, we made three different angled contact between marker 3 and the visual probing device with forces ranging from 1 to 20 N. The displacement errors are presented in Fig. 7(c). The distribution of contact locations when performing perpendicular contact with contact forces of 1, 5, 10, and 20 N is illustrated in Fig. 7(d), which shows the displacement error relative to the true position. At a force of 1 N, the maximum error was 3.5 mm with a standard deviation (SD) of 1.4 mm, which decreased to 0.08 mm as the contact force increased to 20 N. The experimental results indicate that the contact sensing algorithm becomes more stable as the contact force increases. This is attributed to the impact of measurement noise from the F/T sensor. During the movement of US probes, the variations in the contact position are mainly distributed in the low-frequency part. Therefore, for handling low contact forces, it is recommended to utilize a low-pass filter to eliminate the high-frequency components. The fast Fourier transform (FFT) analysis can be used to calculate the cut-off frequency [19], as shown in Fig. 8(a). By implementing a low-pass filter with a cut-off frequency of 10 Hz, as illustrated in Fig. 8(b), the extreme variations in the contact position can be effectively mitigated, thereby improving the robustness of the robot motion control.

Furthermore, to validate the accuracy on different US probes, 15 markers are marked in the same way on the linear probe and convex probe, as shown in Fig. 9(c) and (d), respectively. The displacement error was calculated under the perpendicular contact case, as shown in Fig. 9(a). The accuracy (mean $\pm$ SD) of the T-shaped probe, linear probe and convex probe are 0.94 $\pm$ 0.49 mm, 1.28 $\pm$ 0.44 mm and 0.91 $\pm$ 0.24 mm, respectively. As a result, the contact sensing algorithm has demonstrated robustness in adapting to different probes, with an average error of 1 mm.

C. Performance Evaluation of Contact Force and Angle Control in Dynamic Environment

A soft phantom with a flat surface was mounted on a six-axis platform capable of simulating dynamic environments, as shown in Fig. 5(a). The RUSS was evaluated with regard to force tracking errors in vertical motion, as well as in-plane and out-of-plane angle tracking errors in rotational motion. To simplify calculations, the frames of the six-axis platform and robot base were aligned in parallel. Therefore, the tracking angle between the normal vector of the phantom surface ${}^{P}Z$ and the Z axis of the robot base frame ${}^{B}Z$ was equivalent to the angle of the platform rotation $\theta_p(t)$. Meanwhile, the center scan line of the US probe in the robot base frame ${}^{B}N(t)$ was calculated through the robot forward kinematics model ${}^{B}_{S}T(\theta_j(t))$, where $\theta_j(t)$ represents the joint angles. The real-time angle $\theta_r(t)$ could then be obtained by ${}^{B}N(t)$ and ${}^{B}Z$.

For each experiment, the probe was initially positioned perpendicular to the center of the soft phantom, and the start and end times of the six-axis platform motion were recorded. The data was aligned through timestamps to calculate the tracking errors. The desired contact force was set at 7 N, and the platform's motion in the z-axis direction $Z(t)(mm)$, as well as the angle of rotation $\theta_p(t)(deg)$, followed a sinusoidal pattern. The equation representing this sine motion is as follows.

$$Z(t), \theta_p(t) = 10\sin(0.2\pi t) \tag{11}$$

The vertical position and force tracking errors are presented in Fig. 10(a). The contact force ranged from 5.23 to 8.83 N and the system exhibits a lag in position tracking. This is due to the fact that the admittance controller exhibits a trade-off between stability and responsiveness during parameters tuning. Given

TABLE I
PERFORMANCE OF PROPOSED METHOD ON PHANTOM IN DYNAMIC ENVIRONMENTS (ACCURACY: MEAN)

Method	T=10s		T=5s		T=2s		Measured Signal
	In-Plane	Out-of-Plane	In-Plane	Out-of-Plane	In-Plane	Out-of-Plane	
Human Operators	0.62°	0.83°	1.24°	1.78°	2.87°	3.96°	Human vision and tactile
	1.34°	1.98°	2.69°	3.86°	3.89°	4.62°	Only human tactile
Proposed Method	1.26°	1.55°	3.97°	4.65°	×	×	Only force sensing

TABLE II
PERFORMANCE OF PROPOSED METHOD AND OTHER IFS METHODS (ACCURACY: MEAN ± SD)

Method	T=10s		T=5s		Computational Time	Model Input
	In-Plane	Out-of-Plane	In-Plane	Out-of-Plane		
Proposed method	$1.53° \pm 1.47°$	$1.87° \pm 1.38°$	$3.34° \pm 2.53°$	$3.74° \pm 2.28°$	$0.439ms$	Mesh model
Iterative method	$3.35° \pm 2.54°$	$2.73° \pm 1.40°$	$5.37° \pm 4.15°$	$5.15° \pm 3.89°$	$4.191ms$	Surface Equation
Wrench-axis Method	$2.27° \pm 1.72°$	$2.68° \pm 1.87°$	$4.43° \pm 3.23°$	×	$0.314ms$	Mesh Model

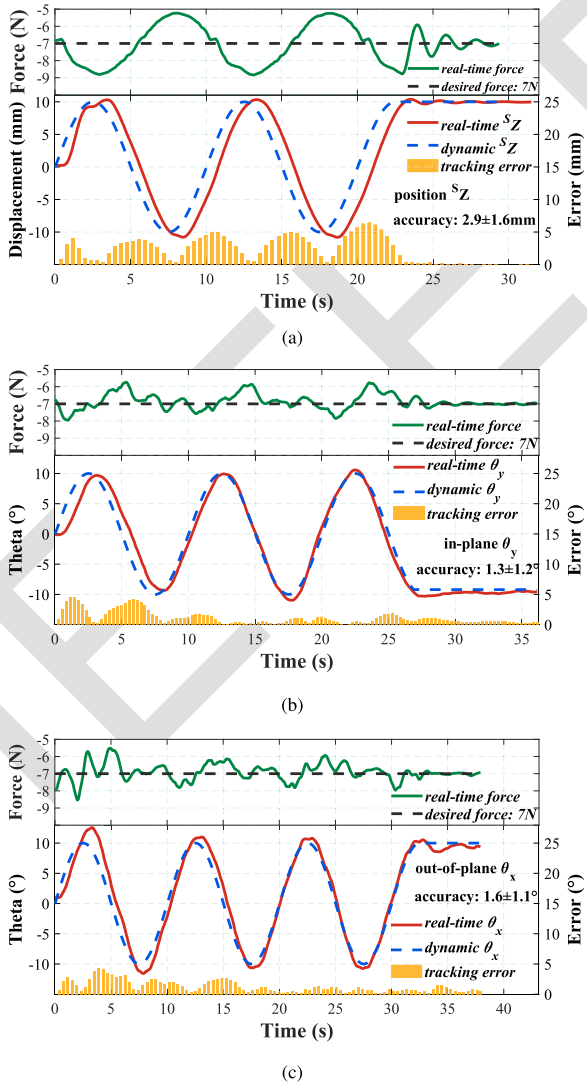

Fig. 10. (a) The contact force and displacements of US probe in the z-axis. (b) The contact force and in-plane angle tracking errors. (c) The contact force and out-of-plane angle tracking errors.

that the US probe will move from initial position to target skin, the model parameters were adjusted to prioritize stability over responsiveness, in order to prevent oscillation during the initial contact. The in-plane and out-of-plane angle tracking errors are depicted in Fig. 10(b) and (c), respectively. The contact force ranged from 6.04 to 8.26 N in the in-plane experiment and from 5.46 to 8.48 N in the out-of-plane experiment. Furthermore, the accuracy (mean ± SD) of angle tracking was $1.3 \pm 1.2°$ and $1.6 \pm 1.1°$ for in-plane and out-of-plane experiments, respectively. These results indicate that the system is capable of maintaining a stable contact force and angle within a dynamic environment.

To further demonstrate the adaptiveness of the proposed method, we conducted comparative experiments in a faster, more dynamic environment. The proposed system is compared with human operators. The experiments involved three human operators who held the probe perpendicular to the phantom, and an AprilTag marker was attached to the probe for visual positioning. To better compare the performance based solely on human tactile perception, we instructed human operators to conduct an additional set of experiments with their eyes closed. As shown in Table I, the angle tracking error increased as the period decreased from 10 to 5 s. The results showed that human operators had a superior ability to maintain stability, particularly in high-speed changing environments. However, the proposed method achieved comparable accuracy to that of human operators while only utilizing force sensing. A cross symbol in Table I indicates that the robot was unable to follow the changes of the phantom, when the six-axis platform moved too quickly ($T = 2\,\mathrm{s}$). This is because the speed limitation of joint and the low control frequency of robot (50 Hz). Although the performance of the proposed method is not as good as that of human operators in high-speed dynamic environments, it demonstrated promising results in maintaining stable contact force and angle.

Then, we further compared our proposed method with existing IFS methods, such as the iteration method and the Wrench-axis method, as shown in Table II. We ensured complete

consistency in all motion control parameters, while varying only the contact sensing model. The iteration method has a primary drawback: it requires an accurate equation for the surface, which is challenging to determine for irregular surfaces like US probes and surgical instruments. Therefore, for this experiment, we were limited to using a convex probe and employed a parabolic surface equation to fit the contact region. Furthermore, the step-by-step iteration process significantly increases the computational time compared to our proposed method. Moreover, the iteration method cannot impose constraints due to using the Levenberg-Marquardt method. On the other hand, the Wrench-axis method fails to account for local deformation and is incapable of handling contact with friction in dynamic environments. The experimental results demonstrated that the proposed method outperforms other methods in dynamic angle tracking performance.

IV. Conclusion

In this letter, we proposed an ultra-fast contact sensing method for arbitrary shaped medical instruments. The novelty lies in the use of a simple multi-plane fitting approach to establish geometric surface descriptions. This method addresses several limitations of intrinsic force sensing algorithm, including high computational time and the inability to adapt to arbitrary surfaces. Point contact with friction experiments were conducted on three commonly used probes (linear probe, convex probe, and T-shaped probe). The experimental results demonstrate that the contact sensing algorithm is robust to friction, and capable of perceiving accurate contact location at high speed (within 1 ms).

However, there are few limitations associated with the current contact sensing algorithm. First, the number of fitted mesh planes should be carefully selected to strike a balance between accuracy and computational time. Second, over prolonged periods of use, the F/T sensor may encounter temperature drift, leading to measurement inaccuracies. As the contact sensing algorithm is highly sensitive to changes in force, it is imperative to employ a stable F/T sensor and a real-time compensation model to mitigate temperature drift. In addition, the current algorithm is unable to handle situations involving multi-point contact, and will only calculate the contact centroid corresponding to the combined external force. To address this limitation, future work will explore the incorporation of additional force sensors to provide redundant F/T measurements, which will help to address complex contact situations.

In clinical US scanning scenarios, it is challenging to avoid human motion, which can result in significant uncertainty. Furthermore, as US imaging is increasingly being utilized in out-of-hospital settings due to its portability, it also presents a challenge to adapt to dynamic environmental changes. Thus, one of the contributions of this work is to equip RUSS with the capability to maintain stable contact force and angle under such dynamic conditions. The experimental results demonstrate that the proposed method can achieve comparable performance with human operators with only force sensing and has the potential to enhance the safety and adaptiveness. Future work aims to enhance the accuracy and robustness of the motion control algorithm in the current RUSS by incorporating proven visual methods and US image information. We believe that our work represents an important step towards the clinical application of real-time contact sensing in medical robots.

References

[1] H. M. Le, T. N. Do, and S. J. Phee, "A survey on actuators-driven surgical robots," *Sensors Actuators A. Phys.*, vol. 247, pp. 323–354, 2016.

[2] M. Bautista, J. Manrique, and W. J. Hozack, "Robotics in total knee arthroplasty," *J. Knee Surg.*, vol. 32, no. 07, pp. 600–606, 2019.

[3] R. S. Dahiya, G. Metta, M. Valle, and G. Sandini, "Tactile sensing-from humans to humanoids," *IEEE Trans. Robot.*, vol. 26, no. 1, pp. 1–20, Feb. 2010.

[4] K. Sun, M. Li, S. Wang, G. Zhang, H. Liu, and C. Shi, "Development of a fiber BRAGG grating-enabled clamping force sensor integrated on a grasper for Laparoscopic surgery," *IEEE Sensors J.*, vol. 21, no. 15, pp. 16681–16690, Aug. 2021.

[5] K. Park, H. Yuk, M. Yang, J. Cho, H. Lee, and J. Kim, "A biomimetic elastomeric robot skin using electrical impedance and acoustic tomography for tactile sensing," *Sci. Robot.*, vol. 7, no. 67, 2022, Art. no. eabm7187.

[6] J. Hu, J. Back, and H. Liu, "A review of tactile sensing in e-skin, wearable device, robotic, and medical service," *Sensory Syst. Robot. Appl.*, vol. 97, 2022, Art. no. 173.

[7] S. Ciotti, T. Sun, E. Battaglia, A. Bicchi, H. Liu, and M. Bianchi, "Soft tactile sensing: Retrieving force, torque and contact point information from deformable surfaces," in *Proc. IEEE Int. Conf. Robot. Automat.*, 2019, pp. 4290–4296.

[8] H. Liu et al., "Finger contact sensing and the application in dexterous hand manipulation," *Auton. Robots.*, vol. 39, pp. 25–41, 2015.

[9] T. Zhang, L. Jiang, X. Wu, W. Feng, D. Zhou, and H. Liu, "Fingertip three-axis tactile sensor for multifingered grasping," *IEEE/ASME Trans. Mechatron.*, vol. 20, no. 4, pp. 1875–1885, Aug. 2015.

[10] U. Kim et al., "Integrated linkage-driven dexterous anthropomorphic robotic hand," *Nature Commun.*, vol. 12, no. 1, 2021, Art. no. 7177.

[11] J. Back, J. Bimbo, Y. Noh, L. Seneviratne, K. Althoefer, and H. Liu, "Control a contact sensing finger for surface haptic exploration," in *Proc. IEEE Int. Conf. Robot. Automat.*, 2014, pp. 2736–2741.

[12] T. Sun and H. Liu, "Adaptive force and velocity control based on intrinsic contact sensing during surface exploration of dynamic objects," *Auton. Robots.*, vol. 44, no. 5, pp. 773–790, 2020.

[13] J. Bimbo, C. Pacchierotti, N. G. Tsagarakis, and D. Prattichizzo, "Collision detection and isolation on a robot using joint torque sensing," in *Proc. IEEE/RSJ Int. Conf. Intell. Robots Syst.*, 2019, pp. 7604–7609.

[14] U. Kim et al., "A novel intrinsic force sensing method for robot manipulators during human–robot interaction," *IEEE Trans. Robot.*, vol. 37, no. 6, pp. 2218–2225, Dec. 2021.

[15] A. Bicchi, J. K. Salisbury, and D. L. Brock, "Contact sensing from force measurements," *Int. J. Robot. Res.*, vol. 12, no. 3, pp. 249–262, 1993.

[16] J. Duffy, "Kinematic geometry of mechanisms (KH HUNT)," *SIAM Rev.*, vol. 33, no. 4, 1991, Art. no. 678.

[17] S. Haddadin, A. De Luca, and A. Albu-Schäffer, "Robot collisions: A survey on detection, isolation, and identification," *IEEE Trans. Robot.*, vol. 33, no. 6, pp. 1292–1312, Dec. 2017.

[18] L.-J. Zhang, R.-Q. Hu, and W.-M. Yi, "Research on force sensing for the end-load of industrial robot based on a 6-axis force/torque sensor," *Acta Automatica Sinica*, vol. 43, no. 3, pp. 439–447, 2017.

[19] Z. Jiang, M. Grimm, M. Zhou, Y. Hu, J. Esteban, and N. Navab, "Automatic force-based probe positioning for precise robotic ultrasound acquisition," *IEEE Trans. Ind. Electron.*, vol. 68, no. 11, pp. 11200–11211, Nov. 2021.

[20] S. R. Buss, "Introduction to inverse kinematics with Jacobian transpose, pseudoinverse and damped least squares methods," *IEEE J. Robot. Automat.*, vol. 17, no. 1–19, 2004. Q4

[21] A. S. B. Mustafa et al., "Development of robotic system for autonomous liver screening using ultrasound scanning device," in *Proc. IEEE Int. Conf. Robot. Biomimetics*, 2013, pp. 804–809.

[22] G. Ma, S. R. Oca, Y. Zhu, P. J. Codd, and D. M. Buckland, "A novel robotic system for ultrasound-guided peripheral vascular localization," in *Proc. IEEE Int. Conf. Robot. Automat.*, 2021, pp. 12321–12327.

[23] Z. Jiang, Y. Zhou, Y. Bi, M. Zhou, T. Wendler, and N. Navab, "Deformation-aware robotic 3D ultrasound," *IEEE Robot. Autom. Lett.*, vol. 6, no. 4, pp. 7675–7682, Oct. 2021.